Supplementary Information on

Spin-defect characteristics of single sulfur vacancies in monolayer MoS_2

A. Hötger,[1] T. Amit,[2] J. Klein,[3] K. Barthelmi,[1] T. Pelini,[4] A. Delhomme,[4] S. Rey,[5] M. Potemski,[4,6] C. Faugeras,[4] G. Cohen,[2] D. Hernangómez-Pérez,[2] T. Taniguchi,[7] K. Watanabe,[8] C. Kastl,[1] J.J. Finley,[1] S. Refaely-Abramson,[2] A.W. Holleitner,[1] and A.V. Stier[1]

[1] *Walter Schottky Institute and Physics Department, TU Munich, 85748 Garching, Germany.*
[2] *Department of Molecular Chemistry and Materials Science, Weizmann Institute of Science, Rehovot, Israel.*
[3] *Department of Materials Science and Engineering, Massachusetts Institute of Technology, Cambridge, Massachusetts 02139, USA*
[4] *Laboratoire National des Champs Magnetiques Intenses, CNRS-UGA-UPS-INSA-EMFL, 38042 Grenoble, France.*
[5] *Department of Photonics Engineering, Technical University of Denmark, 2800 Kgs. Lyngby, Denmark.*
[6] *Institute of Experimental Physics, Faculty of Physics, University of Warsaw, 02-093 Warszawa, Poland*
[7] *International Center for Materials Nanoarchitectonics, National Institute for Materials Science, 1-1 Namiki, Tsukuba 305-0044, Japan.*
[8] *Research Center for Functional Materials, National Institute for Materials Science, 1-1 Namiki, Tsukuba 305-0044, Japan.*

(Dated: December 16, 2022)

SUPPLEMENTARY NOTE 1: SAMPLE CHARACTERIZATION

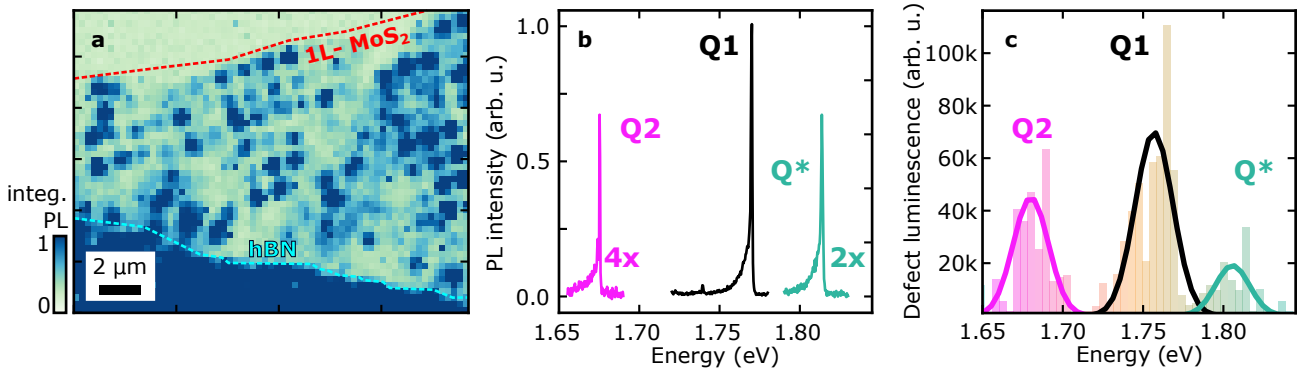

Supplementary Figure 1 | Spatial and energetic distribution of the defect luminescence. a) Spatial map of the defect luminescence integrated from 1.72 to 1.78 eV. The monolayer MoS_2 is located below the red dashed line and is encapsulated in hBN from the turquoise dashed line upwards. Broad backgrounds in the photoluminescence spectra are substracted. Scale bar, 2 µm. b) Typical low-temperature photoluminescence (PL) spectra of the quantum emission Q1, Q2, and Q*. c) Spectral position of the defect luminescence weighted by intensity. Three distinct emission bands are visible. The most prominent is located at ~ 1.75 eV (Q1). Red-shifted to that, at ~ 1.69 eV is the emission band of Q2. The blue-shifted emission band Q* is located at ~ 1.81 eV.

The heterostructure consists of a monolayer MoS_2 encapsulated in multi-layer hexagonal boron nirtide (hBN). The three layers of 2D materials are positioned upon each other by dry viscoelastic stamping methods. Supplementary Figure 1a shows a spatial false color plot of the photoluminescence (PL) integrated from 1.72 to 1.78 eV. The red dashed line illustrates the upper boundary of the MoS_2 flake, whereas the dashed blue line represents the lower boundary of the top hBN flake. The heterostructure, located in between these boundaries, was subsequently irradiated with He-ions. The irradiated pattern is an array of circular patches with a pitch of 2 µm. Optically active defects are generated at the irradiated sites, which appear as sharp emission lines in PL measurements (see Fig S1b). The emission lines are distributed in three distinct clusters Q1, Q2 and Q* (see Supplementary Figure 1c). We attribute emission lines from the later cluster, namely Q*, to adsorbate related defect luminescence[1] and therefore exclude its evaluation from the main manuscript.

Supplementary Figure 2a shows a typical spectrum of the neutral exciton X^A_{1s} of MoS_2. A trion peak appears ~ 30 meV red-shifted to the exciton. We find an inhomogeneous and homogeneous broadening of the lineshape with

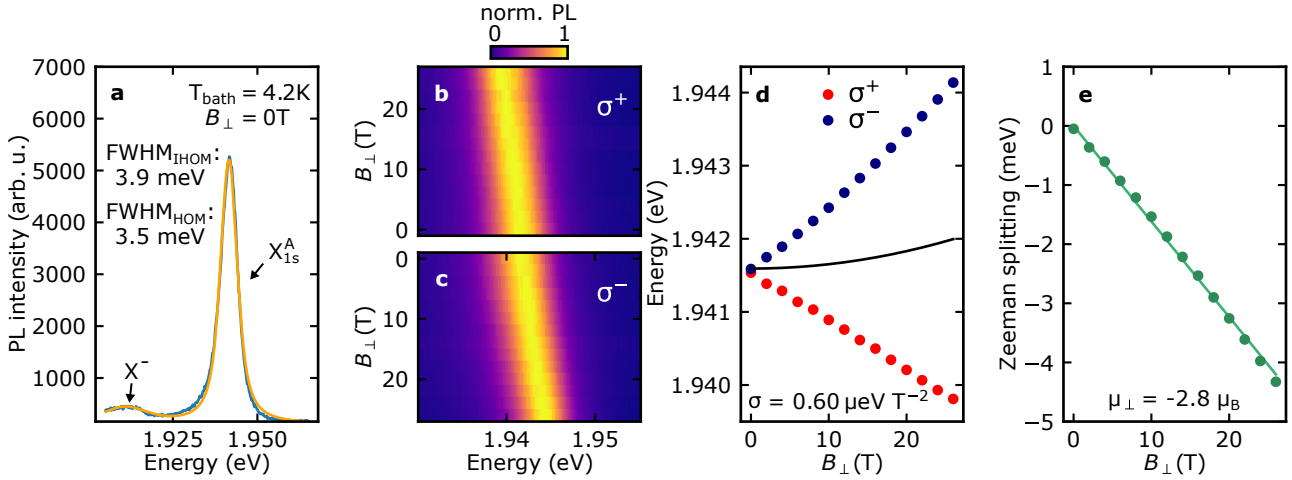

Supplementary Figure 2 | Valley-Zeeman splitting of the neutral exciton in monolayer MoS_2. a) PL spectrum of the neutral exciton with a Voigt fit for exciton X^A_{1s} and trion X^- with an inhomogeneous (3.9 meV) and a homogeneous part (3.5 meV) of the FWHM at $B_\perp = 0$ T and a bath temperature $T_{\mathrm{Bath}} = 4.2$ K. b) - c) Normalized photoluminescence (PL) of the neutral exciton in σ^+ and σ^- detection, respectively. d) Diamagnetic shift of the neutral exciton with $\sigma = 0.60 \pm 0.1\,\mu\mathrm{eV\ T^{-2}}$. e) Valley Zeeman splitting of the neutral exciton with $\mu_\perp = -2.8 \pm 0.1\ \mu_\mathrm{B}$.

3.9 meV and 3.5 meV, respectively. The $B_\perp$ dependent spectra are illustrated as false color plots in Supplementary Figure 2b (c) for σ^+ (σ^-) polarized emission. By fitting the spectral positions we find a diamagnetic shift of $0.6 \pm 0.1\,\mu\mathrm{eV\ T^{-2}}$ (Supplementary Figure 2d) and a valley Zeeman splitting of $\mu_\perp = -2.8 \pm 0.1\ \mu_B$ (Supplementary Figure 2e).

SUPPLEMENTARY NOTE 2: ADDITIONAL OUT-OF-PLANE MAGNETIC FIELD DATA

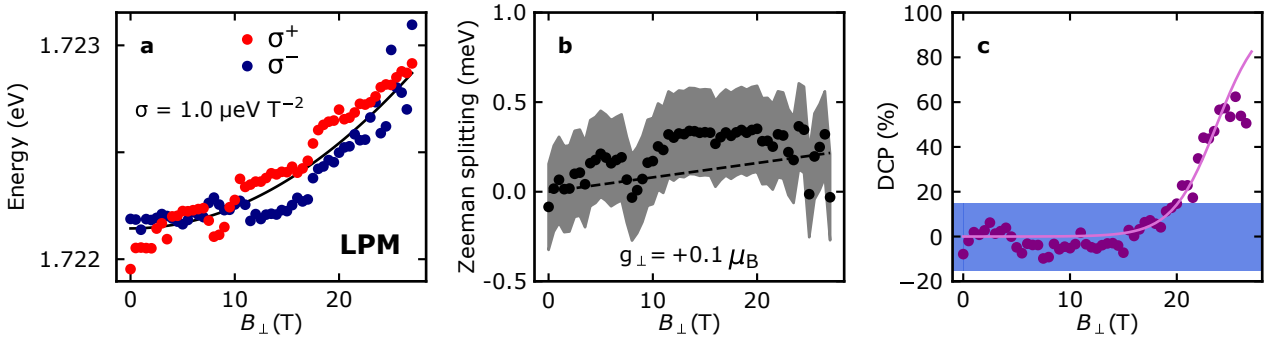

Supplementary Figure 3 | Magneto-spectroscopy on LPM feature. a) Average spectral position of LPM versus $B_\perp$ for σ^+ (red) and σ^- (blue) polarized detected light. A diamagnetic shift of $\sigma = 1.0 \pm 0.1\,\mu\mathrm{eV\ T^{-2}}$ can be extracted. b) Valley Zeeman-splitting of LPM feature ($g_\perp = +0.1 \pm 0.1\ \mu_\mathrm{B}$). c) Degree of circular polarization (DCP) of LPM fitted with equation (1) from the main manuscript.

About 30 meV red-shifted to the quantum emission Q1, we find an additional peak, which we attribute to a local phonon mode (LPM) of the defect center. The magneto-spectroscopy results of the LPM mirror the one of Q1 for the diamagnetic shift (Supplementary Figure 3a), the Zeeman splitting (Supplementary Figure 3b), and the degree of circular polarization (Supplementary Figure 3c).

In total we measured at eight distinct positions on the sample (see Supplementary Figure 6). On three positions we were able to resolve all three emission lines Q1, Q2 and Q*. On five we were able to get signal from emission line

Q1 and Q2 and on the remaining three we only saw Q1. The black dashed lines in the false color plots are guides to the eye for each quantum emission, which resemble Zeeman and diamagnetic shifts evaluated in the main manuscript for Q1, Q2 and Q*. The emitter at position #6 is shown in the main manuscript for the evaluation on Q1. For Q2, we show position #3, in the main manuscript.

Figure S7a) shows the out-of-plane magneto-spectroscopy of the Q* emission (Position #1) in a false color plot. The ZPL of the Q* emission is subject to jitter. The evaluation of the Zeeman splitting is displayed in Supplementary Figure 7b, which reveals a splitting of $g_{\perp,Q^*} = -1.0 \pm 0.1\ \mu_B$. Within the measurement accuracy, we were not able to resolve a diamagnetic shift (see Supplementary Figure 7c). It is reported that the encapsulation of the monolayer MoS_2 fairly reduces the luminescence of Q*. [1]

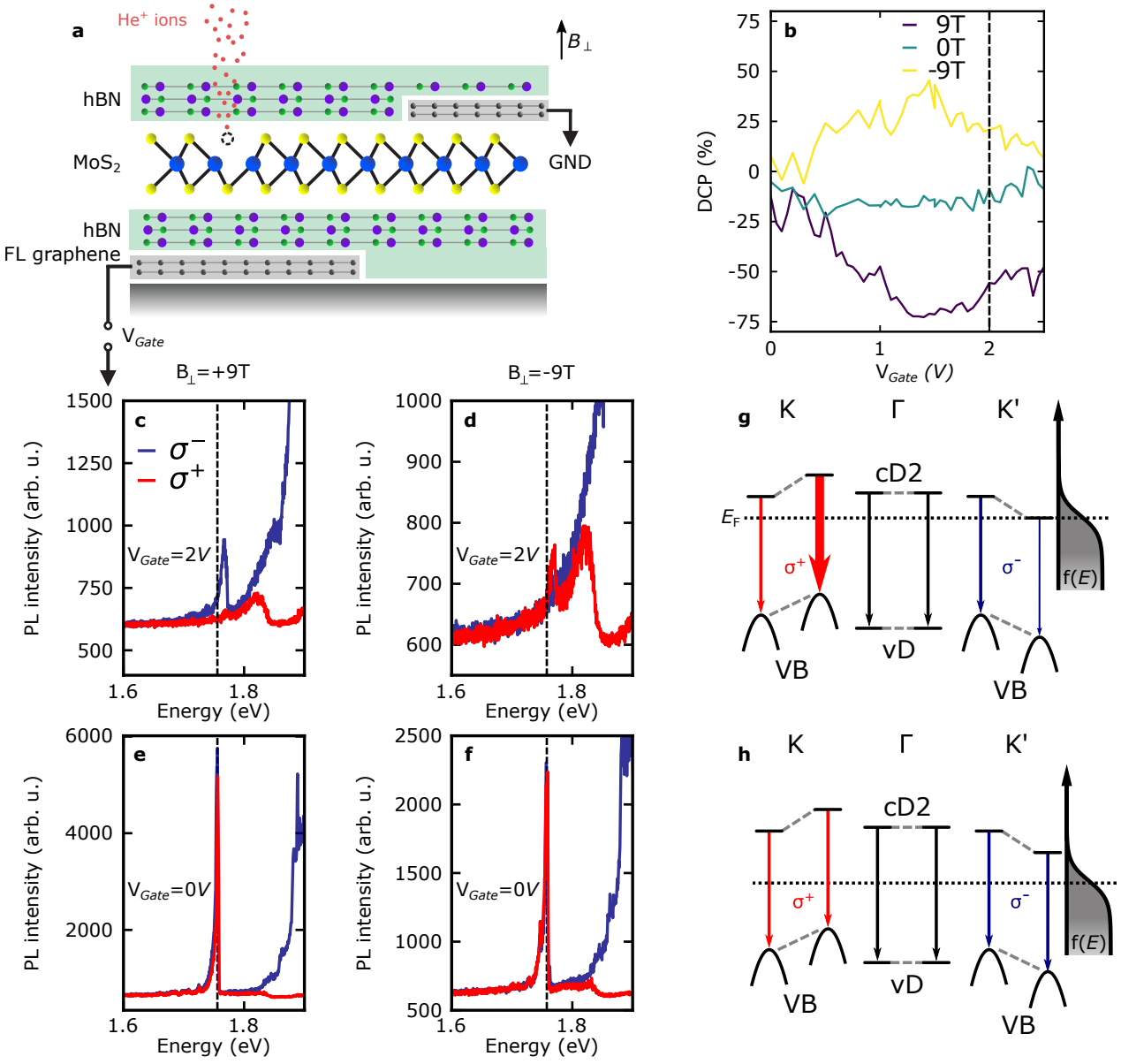

Supplementary Figure 4 | (Figure caption on the next page.)

Supplementary Figure 4 | Degree of circular polarization (DCP) of a Q1-emitter by tuning the Fermi energy E_F and an out-of-plane magnetic field $B_\perp$. a) Sketch of the hBN/MoS_2/hBN heterostructure. Few layer (FL) graphene provides a gate voltage V_{Gate} and contact to the electric ground (GND). b) DCP of Q1 measured as a function of V_{Gate} for $B_\perp = 0\,\mathrm{T}$, $\pm 9\,\mathrm{T}$. c,d) PL spectra of Q1 detected in σ^+ (red) and σ^--polarized (blue) configuration at $V_{\mathrm{Gate}} = 2\,\mathrm{V}$ and $B_\perp = \pm 9\,\mathrm{T}$. e,f) Similar spectra at $V_{\mathrm{Gate}} = 0\,\mathrm{V}$ and $B_\perp = \pm 9\,\mathrm{T}$. The dashed line highlights the energy of the zero-phonon line at $V_{\mathrm{Gate}} = 0\,\mathrm{V}$, indicating a clear blue shift of the emitter at finite V_{Gate}. Experimental parameters: $E_{\mathrm{Laser}} = 1.94\,\mathrm{eV}$, $P_{\mathrm{Laser}} = 1\,\mu\mathrm{W}$, spot size $= 1\,\mu\mathrm{m}$, $T_{\mathrm{Bath}} = 1.7\,\mathrm{K}$. g,h) Sketches of the bandstructure with possible transitions at the high-symmetry points K, Γ and K' for two gate voltages at zero and positive magnetic field. The sketched energy levels summarize the finding of b-f) as follows: The DCP is close to zero for zero gate voltage (and negative voltages) within the given experimental uncertainty [compare b and e,f]. This finding is consistent with the following interpretation: if the Fermi-energy is sufficiently below the unoccupied defect-states, the Zeeman-split states (cD1 and cD2) are equally occupied after an optical excitation and therefore the DCP is negligible [compare b]. At slightly positive gate voltages, the DCP switches sign for negative and positive magnetic fields [compare b and c,d]. This observation suggests that the Zeeman-energy is the relevant energy scale, and the DCP depends on the occupation of the defect bands. For large positive gate voltages, the DCP reduces again [compare b], which is consistent with the spin-split states becoming equally occupied. Importantly, for $V_{\mathrm{Gate}} > 0\,\mathrm{V}$, the Q1 emission shifts to higher energies [compare dashed lines in c,d wrt. e,f]. This blue-shift indicates that in the investigated gate voltage range, the emitters are charge-neutral, while charged free exciton states typically red-shift (including trion and attractive polaron).[2–4] Trion emission from the entire detection spot in the vicinity of Q1 is observed as a background emission at $\approx 1.8eV$ in c and d.

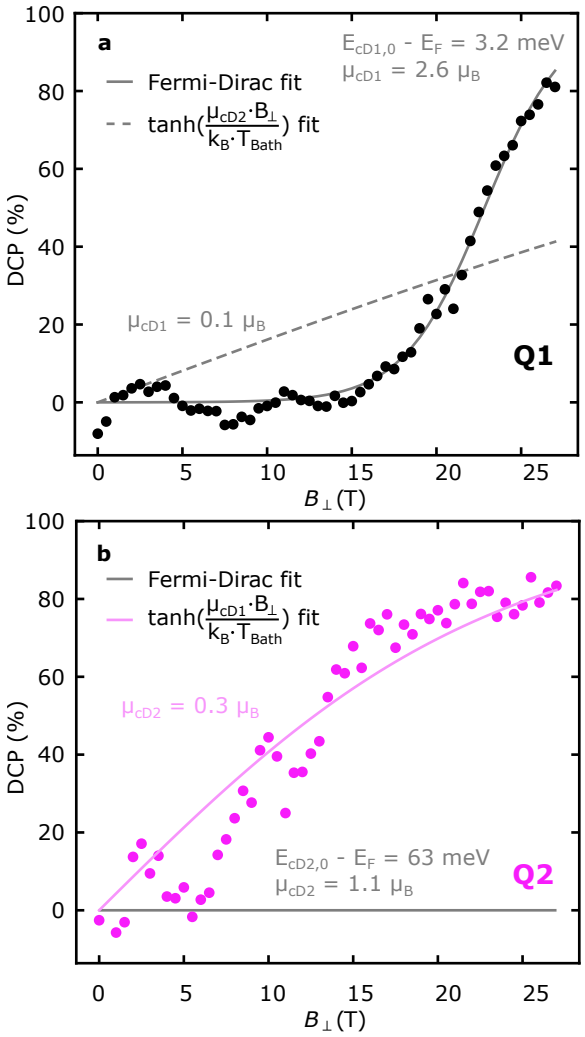

Supplementary Figure 5 | Fits of the DCP versus $B_\perp$ of Q1 and Q2. a) The Fermi-Dirac fit (equation (1), mentioned in the manuscript) fits the DCP data of Q1 well. The fit parameters yield $E_{\mathrm{cD1,0}} - E_{\mathrm{F}} = 3.2\,\mathrm{meV}$ and $\mu_{\mathrm{cD1}} = 2.6\ \mu_{\mathrm{B}}$. However, the tanh $\left(\frac{\mu_{\mathrm{cD2}} \cdot B_\perp}{k_{\mathrm{B}} T_{\mathrm{Bath}}}\right)$ fit is clearly not suitable to describe the data. b) For Q2 we assumed E_{F} to be 63 meV below $E_{\mathrm{cD1,0}}$. The Fermi-Dirac fit cannot map the data points at all. Whereas the tanh $\left(\frac{\mu_{\mathrm{cD1}} \cdot B_\perp}{k_{\mathrm{B}} T_{\mathrm{Bath}}}\right)$ describes the DCP trend with a fitted value of $\mu_{\mathrm{cD1}} = 0.27 \pm 0.01\ \mu_{\mathrm{B}}$. Note, that this value is very sensitive to the bath temperature T_{Bath}, which might explain the discrepancy to the ab-initio calculations ($\mu_{\mathrm{cD1}} = 1.07\ \mu_{\mathrm{B}}$).

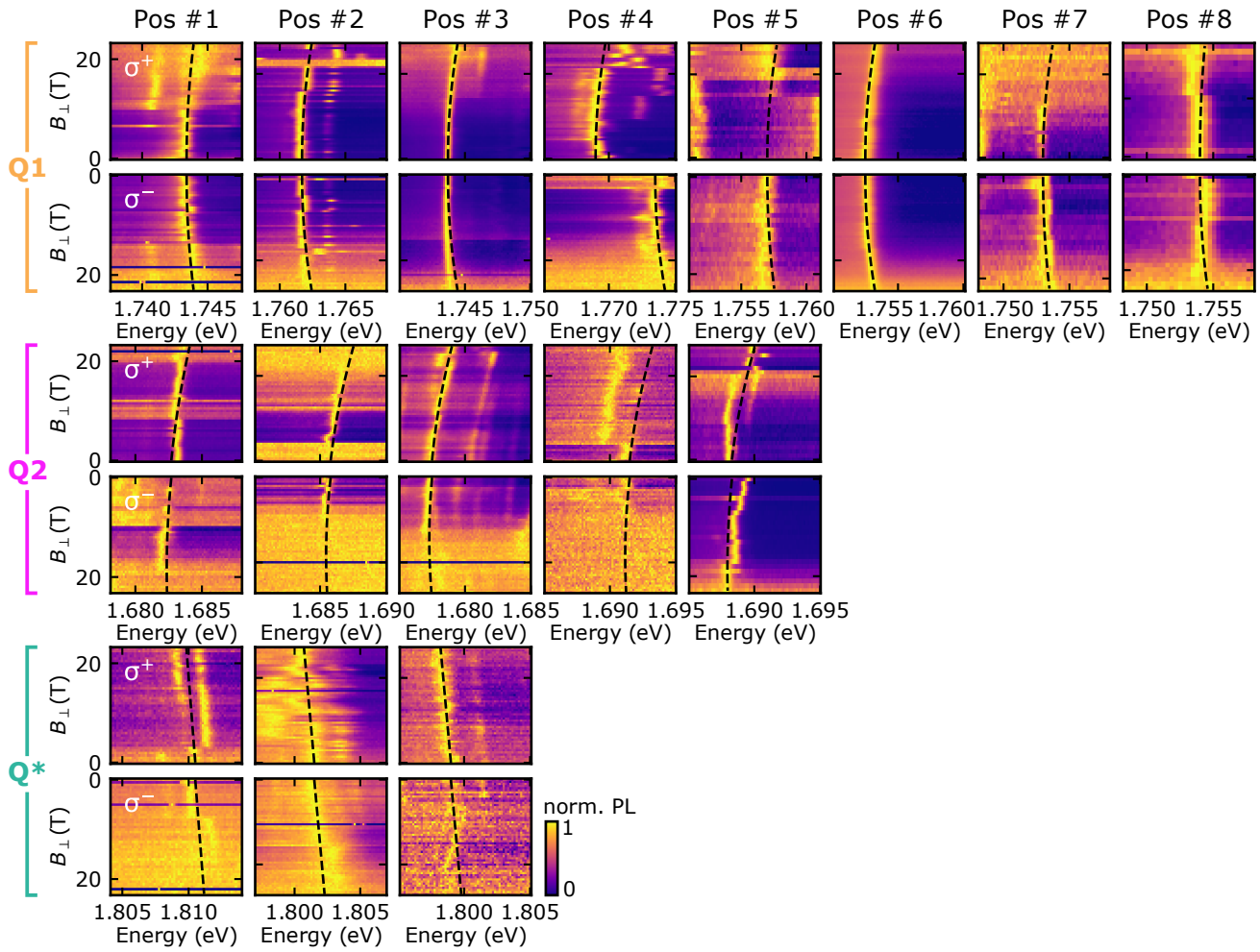

Supplementary Figure 6 | Overview of all magneto-PL measurements in Faraday geometry. The black dashed lines are guides to the eye considering the fitted parameters found for Q1, Q2 and Q*, respectively. For all eight position an emission according to Q1 was found. Additionally at position #1 − #5, an emission conforming to Q2 was found. The quantum emission Q* was found at position #1 − #3. All emitter agree well with the assigned behaviour in magnetic field. Some emitters jitter between different states over time. Nevertheless, their relative shift in magnetic field remains unchanged.

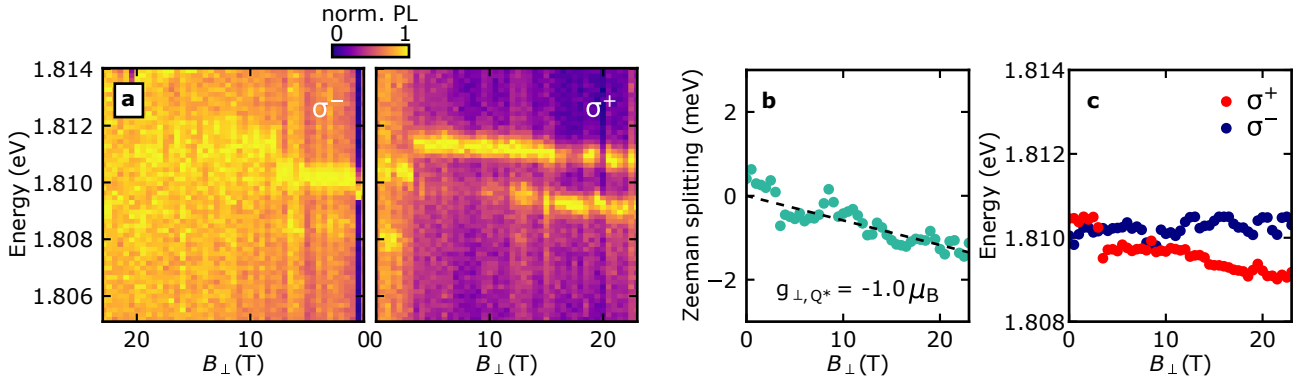

Supplementary Figure 7 | Out-of-plane magneto-spectroscopy on Q* feature. a) False color plot of the spectrum of Q* versus $B_\perp$. The ZPL of the defect luminescence is subject to jitter. b) Zeeman-splitting of Q* feature showing $g_{\perp,Q^*} = -1.0 \pm 0.1\ \mu_B$. c) Average spectral position of LPM versus $B_\perp$ for σ^+ (red) and σ^- (blue) polarized detected light. We find no diamagnetic shift opposing to Q1 and Q2.

SUPPLEMENTARY NOTE 3: ADDITIONAL IN-PLANE MAGNETIC FIELD DATA

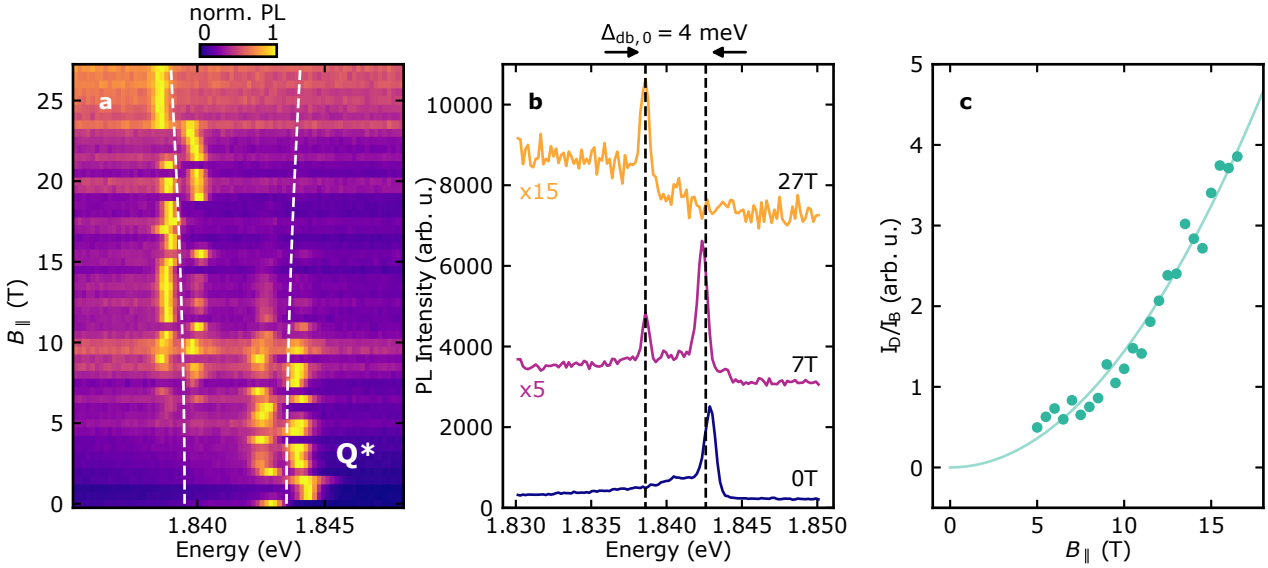

Supplementary Figure 8 | In-plane magneto-spectroscopy on Q* feature. a) False color plot of the PL of Q* versus $B_\parallel$. At $B_\parallel \approx 5\,\mathrm{T}$ a new peak red-shifted to Q* emerges, while the original peak faints out. The white dashed line is calculated with the dark-bright splitting equation mentioned in the main manuscript and uses $|\mu_\parallel| = 1\ \mu_\mathrm{B}$ and $\Delta_\mathrm{DB} = 4\,\mathrm{meV}$. The defect luminescence is subject to jitter, which is further addressed in the Supplementary Figure 9. b) Three distinct spectra at $B_\parallel = 0\,\mathrm{T}$, $7\,\mathrm{T}$, $27\,\mathrm{T}$ showing the original, both, and the brightened defect luminescence, respectively. c) The ratio of the dark and bright emission intensity, reveals a quadratic dependence.

The in-plane magnetic field $B_\parallel$ data on Q* reveals similar to Q2 a brightening of a spin-forbidden dark ground state (see Supplementary Figure 8).

The spectral jitter observable for the Q* emission, can be explained for instance by a dangling adsorbate on a sulfur vacancy. The new branch appearing at finite in-plane magnetic field $B_\parallel$ mirrors the spectral jitter behaviour, when keeping $B_\parallel$ constant (see Supplementary Figure 9).

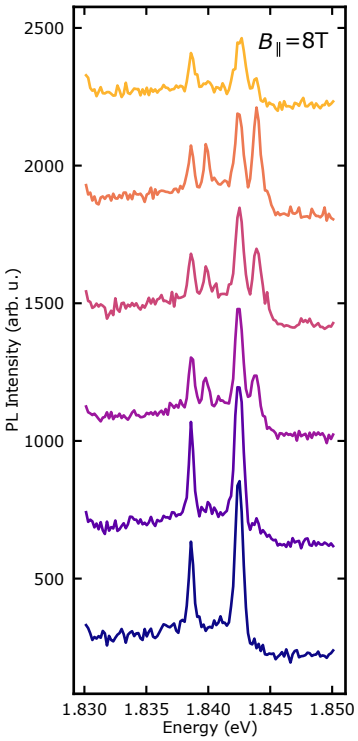

Supplementary Figure 9 | Time trace of a dark and bright quantum emission Q* at constant in-plane magnetic field. Waterfall plot showing six spectra taken one after the other at the same position at a fixed in-plane magnetic field $B_\parallel = 8\,\mathrm{T}$. The jitter of the blue-shifted peak, namely bright quantum emission, resembles the jitter of the dark quantum emission (red-shifted peak). This is another signature for the dark-bright splitting. The dielectric environment, which can vary drastically in real space, is mostly accountable for the jitter seen in the PL. Both emission lines must origin locally from the same position (i.e. seeing the same dielectric environment).

SUPPLEMENTARY NOTE 4: DFT, GW AND BSE CALCULATIONS

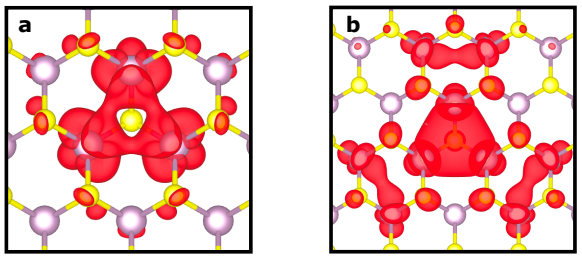

Supplementary Figure 10 | Isosurfaces of the defect wavefunctions. Isosurfaces of the defect electron wavefunction corresponding to defect band a) cD1 and b) vD. The wavefunctions of cD1 and cD2 are similar and are primarily composed of transition metal d-orbitals.

The spin magnetic moment of electronic band n at the reciprocal-space point $\mathbf{k}$ was calculated using:

$$m_{n\mathbf{k}}^{spin} = -\frac{eg_e}{2m_e}\langle\psi_{n\mathbf{k}}|\sigma_z|\psi_{n\mathbf{k}}\rangle, \tag{1}$$

where e is the elementary charge, g_e is the free electron g-factor, namely Zeeman splitting, m_e is the electron's mass, $\psi_{n\mathbf{k}}$ is the wavefunction of band n at k-point $\mathbf{k}$ and σ_z is the Pauli matrix in the $\hat{z}$ direction (perpendicular to the monolayer plane).

The orbital magnetic moment was calculated using:

$$m_{n\mathbf{k}}^{orb} = -\frac{i\mu_B}{m_e}\sum_{n'\neq n}\left(\frac{\langle\psi_{n\mathbf{k}}|\hat{p}_x|\psi_{n'\mathbf{k}}\rangle\langle\psi_{n'\mathbf{k}}|\hat{p}_y|\psi_{n\mathbf{k}}\rangle}{E_{n'\mathbf{k}}-E_{n\mathbf{k}}} - \frac{\langle\psi_{n\mathbf{k}}|\hat{p}_y|\psi_{n'\mathbf{k}}\rangle\langle\psi_{n'\mathbf{k}}|\hat{p}_x|\psi_{n\mathbf{k}}\rangle}{E_{n'\mathbf{k}}-E_{n\mathbf{k}}}\right) \tag{2}$$

Where μ_B is Bohr's magneton, $E_{n\mathbf{k}}$ is the energy of band n at k-point $\mathbf{k}$ and $\hat{p}_i$ is the momentum operator at direction $\hat{i}$.

The spin and orbital parts of the magnetic moment are then added to calculate the total magnetic moment:

$$m_{n\mathbf{k}}^{tot} = m_{n\mathbf{k}}^{spin} + m_{n\mathbf{k}}^{orb}. \tag{3}$$

We extend the single-particle results to a many-body excitonic picture, using the following equation to calculate the g-factor of each exciton based on the GW-BSE results for the excitonic compositions:

$$g^S = \frac{2}{\mu_B}\sum_{vc\mathbf{k}}\left|A_{vc\mathbf{k}}^S\right|^2\left(m_{c\mathbf{k}}-m_{v\mathbf{k}}\right), \tag{4}$$

where $A_{vc\mathbf{k}}^S$ are the GW-BSE exciton coefficients, which weigh the effective-mass transitions.

SUPPLEMENTARY REFERENCES

[1] Klein, J. *et al.*, Engineering the Luminescence and Generation of Individual Defect Emitters in Atomically Thin MoS_2, *ACS Photonics* **8**, 669–677 (2021).

[2] Efimkin, D. K. & MacDonald, A. H., Exciton-polarons in doped semiconductors in a strong magnetic field, *Phys. Rev. B* **97**, 235432 (2018).

[3] Fey, C., Schmelcher, P., Imamoglu, A. & Schmidt, R., Theory of exciton-electron scattering in atomically thin semiconductors, *Phys. Rev. B* **101**, 195417 (2020). 1912.04873.

[4] Hötger, A. *et al.*, Gate-Switchable Arrays of Quantum Light Emitters in Contacted Monolayer MoS_2 van der Waals Heterodevices, *Nano Lett.* **21**, 1040–1046 (2021).